AGGLOMERATION MULTIGRID SIMULATIONS OF TURBULENT VLS FLOWS INCLUDING A PROPULSIVE JET

Daniel Strauss
Instituto Tecnológico de Aeronáutica
CTA/ITA/IEAA
12228-900 – São José dos Campos – SP – BRAZIL
daniel@tecsis.com.br

João Luiz F. Azevedo
Instituto de Aeronáutica e Espaço
CTA/IAE/ASE-N
12228-904 – São José dos Campos – SP – BRAZIL
azevedo@iae.cta.br

A study of the flowfield around axisymmetric launch vehicles in different flight conditions and configurations is performed in this work. Particularly, the VLS second stage configuration is analyzed considering the case with and without a propulsive jet in the vehicle base. The study is performed using a cell centered finite volume formulation on unstructured grids. Different spatial discretization schemes are compared, including a centered and an upwind scheme. The upwind scheme is a second-order version of the Liou flux vector splitting scheme. Turbulence effects are accounted for using two one-equation turbulence closure models, namely the Baldwin and Barth and the Spalart and Allmaras models. An agglomeration multigrid algorithm is used to accelerate the converge to steady-state of the numerical solutions. The numerical results obtained are compared with experimental data as well as with previous structured grid simulations.

Keywords. *Agglomeration Multigrid, Turbulent Flows, Upwind Schemes, VLS.*

1. Introduction

In the context of the development of computational tools for the simulation of launch vehicle flows, previous work (Azevedo, Menezes and Fico, 1995,1996, Azevedo, Strauss and Ferrari, 1999, Strauss and Azevedo, 1999, 2001) by the authors have treated the flowfield around the first Brazilian satellite launcher, the VLS. Viscous turbulent flows in the forebody region (Azevedo, Menezes and Fico, 1995,1996), as well as in the afterbody region (Azevedo, Strauss and Ferrari, 1999, Strauss and Azevedo, 1999) of the vehicle, were considered using a structured grid approach with centered implicit schemes and an axisymmetric formulation. Moreover, an unstructured grid approach was used in order to simulate inviscid flows over the VLS forebody in Strauss and Azevedo (2001). This unstructured grid capability (Strauss and Azevedo, 2001) consisted of an axisymmetric, finite volume, cell centered solver, in which a centered and an upwind scheme where implemented and convergence acceleration was obtained by an agglomeration multigrid procedure. The present work is, then, an extension of the existing capability towards the treatment of viscous turbulent flows over the VLS, including the forebody region and the afterbody region with and without a propulsive jet. Hence, some of the cases studied in Azevedo, Strauss and Ferrari (1999) and Strauss and Azevedo (1999, 2001) are analyzed again with this new implementation.

The unstructured grid approach allows a much larger flexibility in terms of control of computational mesh refinement than a structured grid approach. It can provide a better resolution of flow features with a lower computational cost through the use of adaptive meshes. Moreover, the use of an axisymmetric formulation is indicated due to the axial symmetry of the VLS second stage and to the fact that the vehicle is designed to fly at low angles of attack. In addition, the axisymmetric formulation represents a three-dimensional flow but it has a computational cost equivalent to a two-dimensional simulation. Since high-speed flows including shock waves are among the flows of interest, an upwind spatial discretization scheme is employed in order to increase to solution accuracy. The upwind spatial discretization scheme implemented is a second-order accurate version of Liou's (1994, 1996) AUSM$^+$ scheme. Moreover, the use of one-equation instead of algebraic turbulence closure models is necessary for the adequate solution of the flows of interest, as observed in previous work (Azevedo, Strauss and Ferrari, 1999, Strauss and Azevedo, 1999). The two turbulence closure models treated are the Baldwin and Barth (1990) and the Spalart and Allmaras (1994) models.

The time-stepping method used to advance the solution of the governing equations in time in the present work is a fully explicit, 2nd-order accurate, 5-stage Runge-Kutta scheme (Mavriplis, 1988). As the problems of interest are steady state problems, a variable time stepping option with constant CFL number has been implemented in order to accelerate

convergence. Experimental data and results from a structured mesh solver (Azevedo, Strauss and Ferrari, 1999, Strauss and Azevedo, 1999) are used for comparisons with the present numerical simulations. Comparisons between the results obtained with the centered and the upwind spatial discretization schemes and between the results with the two turbulence closure models implemented are also presented. Solutions over the forebody and over the afterbody regions were obtained and the afterbody region was treated considering cases with and without a propulsive jet.

2. Governing Equations

The governing equations for the aerodynamic flows of interest are the azimuthal-invariant Navier-Stokes equations in cylindrical coordinates, which can be written in integral form for the case of no body rotation as

$$\frac{\partial}{\partial t}\int_V \boldsymbol{Q}\, dV + \int_S \left(\boldsymbol{E}\, rdr - \boldsymbol{F}\, rdz\right) + \int_V \boldsymbol{H}\, dV = 0 \quad . \tag{1}$$

In this expression, r is the radial coordinate, z is the axial coordinate, $\boldsymbol{E} = \boldsymbol{E}^{(i)}$- $\boldsymbol{E}^{(v)}$ and $\boldsymbol{F} = \boldsymbol{F}^{(i)}$- $\boldsymbol{F}^{(v)}$. Moreover, $\boldsymbol{Q}$ is the vector of conserved properties, $\boldsymbol{E}^{(i)}$ and $\boldsymbol{F}^{(i)}$ are the inviscid flux vectors, $\boldsymbol{E}^{(v)}$ and $\boldsymbol{F}^{(v)}$ are the viscous flux vectors and $\boldsymbol{H}$ is the axisymmetric source term. The definition of these terms is

$$\boldsymbol{Q} = \begin{Bmatrix} r \\ r u_z \\ r u_r \\ e \end{Bmatrix}, \quad \boldsymbol{H} = \begin{Bmatrix} 0 \\ 0 \\ -p/r \\ 0 \end{Bmatrix}, \quad \boldsymbol{E}^{(v)} = \frac{M_\infty}{Re}\begin{Bmatrix} 0 \\ t_{zz} \\ t_{zr} \\ t_{zz}u_z + t_{zr}u_r - q_z \end{Bmatrix},$$

$$\boldsymbol{E}^{(i)} = \begin{Bmatrix} r u_z \\ r u_z^2 + p \\ r u_z u_r \\ (e+p)u_z \end{Bmatrix}, \quad \boldsymbol{F}^{(i)} = \begin{Bmatrix} r u_r \\ r u_z u_r \\ r u_r^2 + p \\ (e+p)u_r \end{Bmatrix}, \quad \boldsymbol{F}^{(v)} = \frac{M_\infty}{Re}\begin{Bmatrix} 0 \\ t_{zr} \\ t_{rr} \\ t_{zr}u_z + t_{rr}u_r - q_r \end{Bmatrix}. \tag{2}$$

In the previous expressions, r is the density, u_r and u_z are the velocity components, p is the static pressure, e is the total energy, t_{ij} are the components of the viscous stress tensor and q_i are the heat flux components. Moreover, a suitable nondimensionalization of the governing equations is assumed in order to write Eq. (2). In the present case, the choice of reference state proposed in Pulliam and Steger (1980) is adopted. In this equation, M_∞ is the freestream Mach number and the Reynolds number is defined in its usual form as

$$Re = \frac{l r_\infty q_\infty}{m_\infty} \quad . \tag{3}$$

where l is the reference length, r_∞ is the freestream density, q_∞ is the magnitude of the freestream velocity vector, and m_∞ is the molecular viscosity coefficient at the freestream temperature.

With the use of a cell centered based finite volume scheme, the discrete conserved variable vector is defined as an average over the cell of the continuous properties. Hence, for the *i-th* volume, the discrete property vector is

$$\boldsymbol{Q}_i = \frac{1}{V_i}\int_{V_i} \boldsymbol{Q}\, dV \quad . \tag{4}$$

The definition of the discrete vector $\boldsymbol{Q}_i$ can be used to rewrite Eq. (1), resulting in the equation that has to be numerically implemented, that is

$$\frac{\partial}{\partial t}\left(V_i \boldsymbol{Q}_i\right) + \int_{S_i}\left(\boldsymbol{E}\, rdr - \boldsymbol{F}\, rdz\right) + V_i \boldsymbol{H}_i = 0 \quad , \tag{5}$$

where $\boldsymbol{H}_i = \boldsymbol{H}(\boldsymbol{Q}_i)$.

3. Turbulence Modeling

The correct account for the viscous effects in the present case involves the implementation of an appropriate turbulence closure model. The turbulence closure models implemented in this work were the Baldwin and Barth (1990) and the Spalart and Allmaras (1994) one-equation models. These models attempt to avoid the need to compute algebraic length scales, without having to resort to more complex two-equation, or κ - ε - type models. The models were implemented in the present code precisely as described in Baldwin and Barth (1990) original work and in Spalart and Allmaras (1994) original work for the case with no laminar regions.

The extension of both models for compressible flows was obtained simply by multiplying the kinematic turbulent viscosity coefficient by the local density, as indicated in Baldwin and Barth (1990) and Spalart and Allmaras (1994). Moreover, the turbulence model equation is solved separately from the other governing equations in a loosely coupled fashion.

The Baldwin and Barth model partial differential equation, observing the nondimensionalization adopted, is

$$\frac{D\left(\mathbf{n}\tilde{R}_T\right)}{Dt} = \left(c_{e_2}f_2 - c_{e_1}\right)\sqrt{\mathbf{n}\tilde{R}_T P} + + \frac{M_\infty}{Re}\left[\left(\mathbf{n}_l + \frac{\mathbf{n}_t}{\mathbf{s}_e}\right)\nabla^2\left(\mathbf{n}\tilde{R}_T\right) - \frac{1}{\mathbf{s}_e}(\nabla\mathbf{n}_t)\cdot\nabla\left(\mathbf{n}\tilde{R}_T\right)\right]. \tag{6}$$

In the previous equation $\frac{D}{Dt}(\ ) = \frac{\partial}{\partial t}(\ ) + \mathbf{V}\cdot\nabla(\ )$ is the material derivative, which contains the time derivative and convective terms, the first term on the right hand side of the equation is the production term and the terms between the brackets are the diffusion terms. This equation is solved for the variable $\left(\mathbf{n}\tilde{R}_T\right)$ and the eddy viscosity is calculated as

$$\mathbf{m}_t = \mathbf{r}\, c_{\mathbf{m}} D_1 D_2 \left(\mathbf{n}\tilde{R}_T\right) \ , \tag{7}$$

where the damping functions D_1 and D_2 are designed to allow the model to be used in the near-wall region and are given by

$$D_1 = 1 - \exp\left(-\mathbf{h}^+ / A_1^+\right), \qquad D_2 = 1 - \exp\left(-\mathbf{h}^+ / A_2^+\right) \ , \tag{8}$$

with

$$\mathbf{h}^+ = \sqrt{\frac{Re}{M_\infty}\frac{\mathbf{t}_w}{\mathbf{r}_w}\frac{d}{\mathbf{n}}} \ \ . \tag{9}$$

Here, d is the distance to the wall and

$$P = \mathbf{n}_t\left(\frac{\partial u_i}{\partial x_j} + \frac{\partial u_j}{\partial x_i}\right) - \frac{2}{3}\mathbf{n}_t\left(\frac{\partial u_k}{\partial x_k}\right)^2 \ \ . \tag{10}$$

In the previous equation, the usual Einstein notation and sum convention are used. The symbols u_i and x_i denotes the components of the velocity vector and coordinate system directions, respectively. Furthermore, $\mathbf{n}_t = \mathbf{m}_t/\mathbf{r}$ is the equivalent of a kinematic eddy viscosity,

The Spalart and Allmaras model partial differential equation, observing the nondimensionalization adopted, is

$$\frac{D\tilde{\mathbf{n}}}{Dt} = c_{b1}\tilde{S}\tilde{\mathbf{n}} + \frac{M_\infty}{Re}\left\{\frac{1}{\mathbf{s}}\left[\nabla.\left((\mathbf{n}+\tilde{\mathbf{n}})\nabla\tilde{\mathbf{n}}\right) + + c_{b2}(\nabla\tilde{\mathbf{n}})^2\right] - c_{w1}f_w\left[\frac{\tilde{\mathbf{n}}}{d}\right]^2\right\} \ \ . \tag{11}$$

Again, $\frac{D}{Dt}(\ )$ is the material derivative and the first term on the right hand side of the equation is the production term. Moreover, the last term of the equation is the destruction term and the other terms are the diffusion terms. This equation is solved for the variable $\tilde{\mathbf{n}}$ and the eddy viscosity is calculated as

$$\mathbf{m}_t = \mathbf{r}\tilde{\mathbf{n}}f_{v1} \ , \tag{12}$$

where the function f_{v1} is a damping function used to properly treat the buffer layer and viscous sublayer and it is given by

$$f_{v1} = \frac{\mathbf{c}^3}{\mathbf{c}^3 + c_{v1}^3} \ , \tag{13}$$

where

$$\mathbf{c} \equiv \frac{\tilde{\mathbf{n}}}{\mathbf{n}} \ \ . \tag{14}$$

The production term is based on the vorticity and it can be written as

$$\tilde{S} \equiv S + \frac{M_\infty}{Re}\frac{\tilde{\mathbf{n}}}{k^2 d^2}f_{v2} \ , \tag{15}$$

where

$$S = |\boldsymbol{w}| = \sqrt{\Omega_{ij}\Omega_{ij}} \quad , \tag{16}$$

and the rotation tensor $\boldsymbol{W}_{ij}$ is given by

$$\Omega_{ij} = \frac{\partial u_i}{\partial x_j} - \frac{\partial u_j}{\partial x_i} \quad . \tag{17}$$

4. Spatial Discretization Schemes

The purpose of the spatial discretization scheme is to numerically evaluate the surface integral in Eq. (5). This approximation of the integral is different for the inviscid and for the viscous flux terms. In this work, while the viscous terms are always treated using a centered scheme, the inviscid terms are treated using a centered or an upwind scheme. The approximation of the integral of the inviscid flux vectors is called convective operator, which is defined as

$$C(\boldsymbol{Q}_i) \cong \int_{S_i} \left(\boldsymbol{E}^{(i)} r dr - \boldsymbol{F}^{(i)} r dz \right) = \sum_{k=1}^{n} \left[\boldsymbol{E}_{ik}^{(i)} r_{ik} \boldsymbol{D} r_{ik} - \boldsymbol{F}_{ik}^{(i)} r_{ik} \boldsymbol{D} z_{ik} \right] \quad . \tag{18}$$

Similarly, the approximation of the integral of the viscous flux vectors is called viscous operator, and is defined as

$$V(\boldsymbol{Q}_i) \cong \int_{S_i} \left(\boldsymbol{E}^{(v)} r dr - \boldsymbol{F}^{(v)} r dz \right) = \sum_{k=1}^{n} \left[\boldsymbol{E}_{ik}^{(v)} r_{ik} \boldsymbol{D} r_{ik} - \boldsymbol{F}_{ik}^{(v)} r_{ik} \boldsymbol{D} z_{ik} \right] \quad . \tag{19}$$

For the centered scheme, the convective operator can be written as

$$C(\boldsymbol{Q}_i) = \sum_{k=1}^{n} \left[\boldsymbol{E}^{(i)}(\boldsymbol{Q}_{ik}) r_{ik} \boldsymbol{D} r_{ik} - \boldsymbol{F}^{(i)}(\boldsymbol{Q}_{ik}) r_{ik} \boldsymbol{D} z_{ik} \right] \quad , \tag{20}$$

where $\boldsymbol{Q}_{ik}$ is the arithmetic average of the conserved properties in the cells which share the ik interface, and n is the number of edges that form the i-th control volume. The terms Δr_{ik}, Δz_{ik} and r_{ik} are calculated as

$$\Delta r_{ik} = r_{n2} - r_{n1} \quad , \qquad \Delta z_{ik} = z_{n2} - z_{n1} \quad , \qquad r_{ik} = \frac{r_{n1} + r_{n2}}{2} \quad , \tag{21}$$

where (z_{n1}, r_{n1}) and (z_{n2}, r_{n2}) are the vertices which define the interface between cells i and k. A schematic representation of the nodes and edge nomenclature is presented in Figure 1.
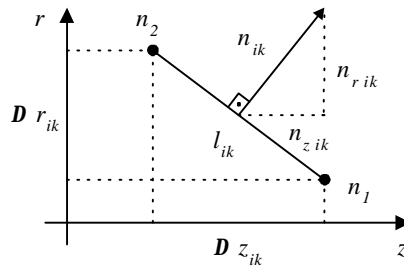

Figure 1: Nodes and edge nomenclature.

The spatial discretization procedure presented in Eq. (20) is equivalent to a central difference scheme. Therefore, artificial dissipation terms must be added in order to control nonlinear instabilities (Jameson and Mavriplis, 1986). In the present case, the artificial dissipation operator is formed as a blend of undivided Laplacian and biharmonic operators (Mavriplis, 1988,1990). Moreover, the scaling terms of the artificial dissipation model were implemented following two approaches: Jameson and Mavriplis' (1986) work and Mavriplis' (1990) work.

The Liou scheme implementation follows the work in Strauss and Azevedo (2001) and Azevedo and Korzenowski (1998) for both the first and second order version of the scheme. The second order version of the scheme is obtained by following exactly the same formulation of the first order version, except that the left and right states are obtained by a MUSCL extrapolation of primitive variables (van Leer, 1979). In Azevedo and Korzenowski (1998), a one-dimensional stencil normal to the control volume edge is constructed in order to obtain the extrapolated interface properties. In this work, cell averaged property gradients are computed and used to calculate the extrapolated properties (Barth and

Jespersen, 1989), which is a different approach from that used in Azevedo and Korzenowski (1998). With the property extrapolation, the state variables are represented as piecewise linear within each cell, instead of piecewise constant. Hence, in order to avoid oscillations in the solution due to the property extrapolation, it is necessary to use a limiter. The minmod limiter was implemented, following the work in (Barth and Jespersen, 1989). Moreover, the limiter value is "frozen" after a certain number of iterations in order to obtain a better convergence rate, as described in Venkatakrishnan (1995).

A centered discretization scheme was also used for the viscous operator, such that it can be written as

$$V\left(\boldsymbol{Q}_i\right) = \sum_{k=1}^{n}\left[\boldsymbol{E}^{(v)}\left(\boldsymbol{Q}_{ik}, \left(\frac{\partial \boldsymbol{Q}}{\partial x_i}\right)_{ik}\right) r_{ik}\,\boldsymbol{D}r_{ik} - \boldsymbol{F}^{(v)}\left(\boldsymbol{Q}_{ik}, \left(\frac{\partial \boldsymbol{Q}}{\partial x_i}\right)_{ik}\right) r_{ik}\,\boldsymbol{D}z_{ik}\right] . \qquad (22)$$

In the previous expression, $\boldsymbol{Q}_{ik}$ is, again, the arithmetic average of the conserved properties in the cells which share the ik interface and $\left(\dfrac{\partial \boldsymbol{Q}}{\partial x_i}\right)_{ik}$ is the arithmetic average of the conserved properties derivatives in the cells which share the ik interface. These derivatives are computed in each volume considering that the discrete derivative in a given volume is the average on the volume of the derivative, and then using Green's theorem to transform the computation of the derivative into the computation of a line integral.

5. Multigrid Implementations

The agglomeration multigrid (Mavriplis, 1994) procedure was selected among the different options of multigrid implementation on unstructured meshes (Mavriplis, 1988, 1990, 1994). This approach does not present the mesh limitations of a nested grid approach (Mavriplis, 1988) nor the complexity of the calculation of the mesh intersections on a non-nested grid approach(Mavriplis, 1988, 1990). Moreover, it provides a fully automatic generation of the coarse meshes in such a way that only the fine mesh has to be provided as input data. Furthermore, the agglomeration multigrid approach maintains the convergence acceleration characteristics of the other multigrid procedures.

Since an agglomeration multigrid strategy was selected, the coarse meshes for the multigrid procedure are generated by agglomerating or grouping fine mesh volumes to form one coarse mesh volume. A "seed" volume is chosen in the fine mesh and, then, all the volumes that have a node or an edge in common with this "seed" volume are grouped and they form the coarse mesh volume. Another "seed" volume is selected and the agglomeration procedure continues grouping all the fine mesh volumes. It should be noted that during the agglomeration procedure only the volumes that have not been already agglomerated may be grouped to form a coarse mesh volume. This is a necessary condition in order to guarantee that there is no volume overlapping in the coarse mesh.

Better coarse mesh quality can be obtained if the selection of the "seed" volumes is not random. Therefore, a list containing all the fine mesh volumes is generated prior to the agglomeration procedure. In this work, the list is formed such that the first entries are the volumes next to a boundary. This approach is very simple, easy to implement and adds very little computational cost. Although it does not necessarily provide the best agglomeration of the interior volumes, it results in good quality coarse mesh volumes close to the boundaries.

As the spatial discretization scheme used in this work is linear, a simplification can be made in the coarse meshes. This simplification consists in eliminating the nodes that belong to only two volumes. The justification for this procedure comes from the fact that the flux passing between the two volumes is the same whether the boundary separating the two volumes is discretized by one or many edges, provided that the discretization scheme is linear. Therefore, a significant amount of storage space can be saved by performing this mesh simplification. Figure 2 presents an example of such node elimination, where the darker lines represent the original boundary separating two coarse volumes and the dashed line represents the boundary edge after the node elimination.
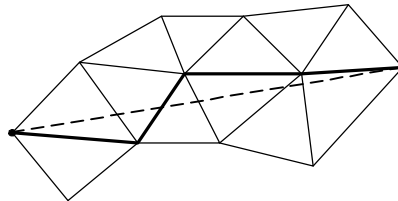

Figure 2: Mesh simplification by the node elimination procedure.

Although the mesh simplification previously described can reduce the total storage space required by the code, it brings a complication related to the connectivity of the nodes in the mesh. As some nodes in the mesh are not used, it is necessary to ensure that the remaining nodes are properly counterclockwise oriented in order to have the normal vectors of each edge correctly pointing outwards. This is accomplished using the node orientation in the fine mesh volumes to direct the ordering of the nodes in the coarse mesh volumes.

The agglomeration procedure can be summarized, then, in three steps. The first step consists in defining the list of volumes of the fine mesh. In the second step, the fine mesh volumes are agglomerated to form the coarse mesh

volumes, following the list generated in the first step. During this step, the mesh simplification described is adopted, and only the nodes that belong to three or more coarse mesh volumes are stored. The third and final step is the verification of the node orientation in each volume of the coarse mesh, and the correction of the orientation where it is needed. The actual implementation of this agglomeration procedure was designed to require the minimum amount of storage possible. Therefore, the only extra information that has to be stored in each mesh, besides the usual information associated with the solution procedure, is the number of the coarse mesh volume that contains each of the fine mesh volumes.

In the multigrid procedure, the restriction operator transfers a variable from a fine mesh to a coarse mesh. The operator used in the present work for the conserved property restriction is the volume weighted average. Therefore, the restricted conserved properties of a coarse mesh volume are equal to the sum of the conserved properties of all the fine mesh cells that form this coarse mesh volume, weighted by their volumes. On the other hand, the restriction of the residuals is accomplished by simple addition of the fine mesh residuals. Hence, the residual of a coarse mesh volume is equal to the sum of the residuals of all the fine mesh volumes that are contained by this coarse mesh volume. The restriction operator for the residuals is different from the restriction operator for the conserved properties because the residuals can be interpreted as line integrals in finite volume schemes. Consequently, as the residuals of the fine mesh are summed, the interior edges contribution will cancel each other, leaving only the contribution of the edges that form the coarse mesh volume.

The prolongation operator, in opposition to the restriction operator, transfers a variable from a coarse mesh to a fine mesh. As usual with typical multigrid implementation, only the conserved property corrections have to be prolonged. Hence, only one prolongation operator has to be defined. In this work, an averaging operator was used to obtain the corrections in the fine grids. The averaging operator consists in, for each edge of the fine mesh, arithmetically averaging the corrections of the coarse mesh volumes corresponding to the two volumes that contain the edge. For each volume, then, these averaged corrections are summed and the result is divided by the number of edges of the volume. This operator is very easy to implement, and it has the advantage of being able to transfer a linear distribution with less error than a direct injection prolongation operator.

6. Results and Discussion

The computational mesh used in the forebody cases is presented in Figure 3 and the corresponding agglomerated meshes used for the multigrid procedure are also shown in this figure. Although this mesh is composed of quadrilateral cells and could be used in a structured mesh approach, the authors emphasize that this mesh was treated in a fully unstructured fashion. Actually, the computational grids used in the present work are the same used in Azevedo, Strauss and Ferrari (1999) and Strauss and Azevedo (1999, 2001) in order to allow a direct comparison between the present results and the results obtained in these references.
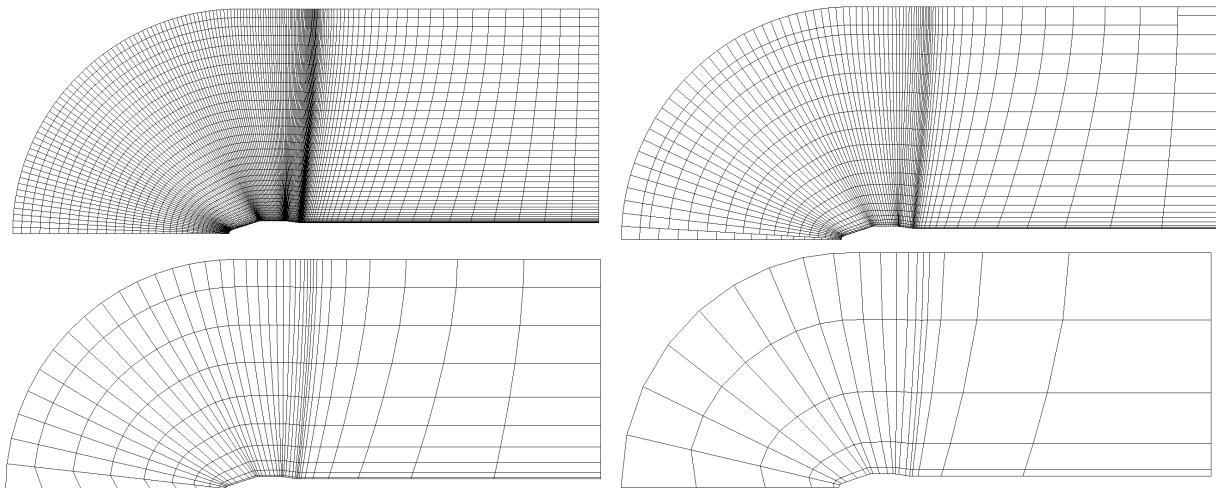

Figure 3: Computational mesh for the VLS forebody and three agglomerated meshes obtained from this mesh.

A comparison of pressure coefficient distributions over the VLS for the cases using the centered scheme and both the Baldwin and Barth and the Spalart and Allmaras turbulence closure models is presented in Figure 4. This case considers $M_\infty = 0.90$ and viscous turbulent flow with $Re = 20 \times 10^6$. In this figure, the Baldwin and Barth model results are indicated by B-B, while the Spalart and Allmaras model results are indicated by S-A. Moreover, for the simulations shown in Figure 4, Jameson and Mavriplis' artificial dissipation model is used in all cases except for one, in which Mavriplis' model is used. The pressure coefficient distribution for the Euler case presented in Strauss and Azevedo (2001) is also shown in Figure 4. The results for both the Baldwin and Barth and Spalart and Allmaras turbulence closure models are very similar and they are also similar to the Euler results. Nevertheless, the viscous turbulent cases do not present the overexpansion and overcompression shown by the Euler results at the forebody cylinder-boattail

intersection region and at the boattail-afterbody cylinder intersection region, respectively. Moreover, the results using Mavriplis' artificial dissipation model instead of Jameson and Mavriplis' model are in better agreement with the experimental results than the other results presented in Figure 4.
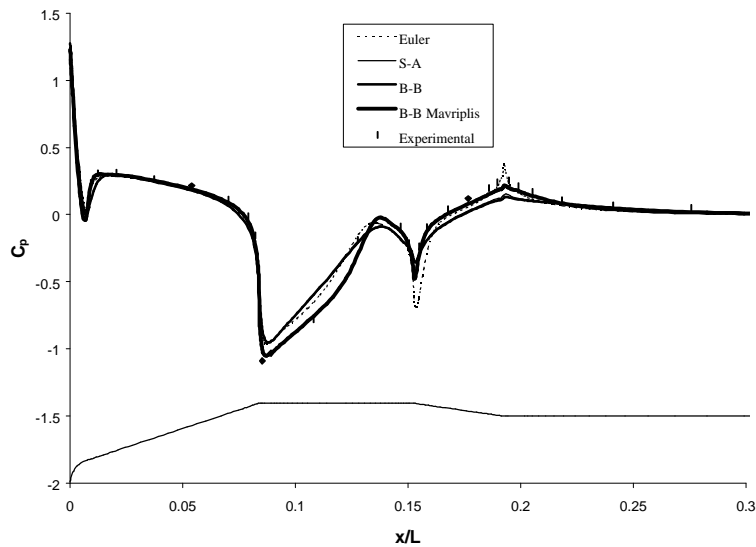

Figure 4: Comparison of pressure coefficient distributions with the centered scheme($M_\Psi = 0.90$ and $Re = 20 \times 10^6$). Jameson and Mavriplis' artificial dissipation model is used wherever nothing is stated.

The results obtained with Liou's spatial discretization scheme and both the Baldwin and Barth and the Spalart and Allmaras models are presented in Figure 5. The corresponding results for the inviscid case, presented in Strauss and Azevedo (2001), as well as the results with the centered scheme with Mavriplis' artificial dissipation model, presented in Figure 4, are also shown in Figure 5. As observed in the inviscid cases (Strauss and Azevedo, 2001), the Liou scheme provides a numerical solution with better comparison with the experimental data than the solution with the centered scheme. However, the solution with the centered scheme and Mavriplis' artificial dissipation model is very close to the solution with Liou's scheme. Moreover, similarly to the observed with the centered scheme, the results with the turbulence models do not present the overexpansion and overcompression observed in the inviscid results.
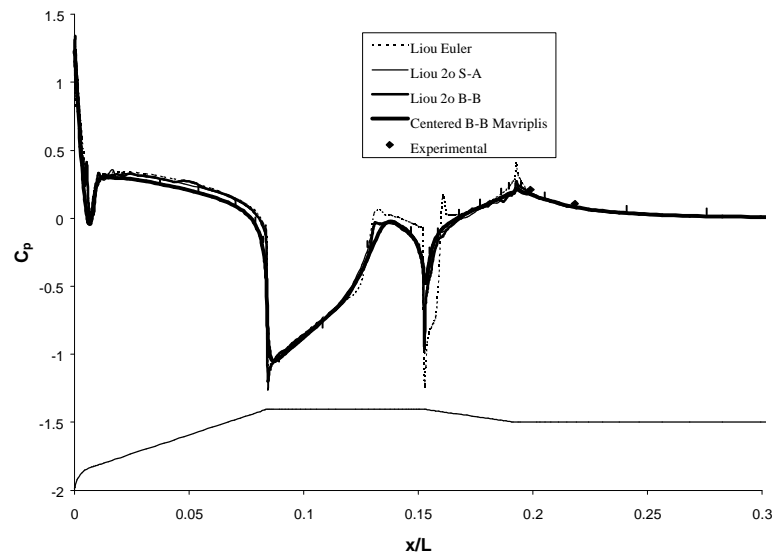

Figure 5: Pressure coefficient distributions with Liou's second order scheme ($M_\Psi = 0.90$ and $Re = 20 \times 10^6$).

Another important result obtained for the viscous turbulent case is the turbulent viscosity distribution on the flowfield. Hence, the turbulent viscosity contours for the case using Liou's spatial discretization scheme and the Spalart and Allmaras turbulence closure model are presented in Figure 6. In this figure one can observe that meaningful values of turbulent viscosity are concentrated in the boundary layer close to the body, where the shear stresses are relevant. Moreover, the boundary layer thickens from the forebody to the afterbody. This behavior is exactly the expected one for this case. A result similar to that of Figure 6 was obtained with the Baldwin and Barth turbulence closure model, although some oscillations in the turbulence viscosity were observed at the edge of the boundary layer.

Figure 6: Turbulent viscosity contours for the case with Liou's second order scheme and the Spalart and Allmaras model ($M_{\Psi} = 0.90$ and $Re = 20 \times 10^6$).

The mesh used to obtain the last results presented for the VLS was the mesh presented in Figure 3. As already mentioned, this mesh was generated from a structured mesh. This structured mesh was, then, used to obtain numerical results for the same case with $M_{\Psi} = 0.90$ and $Re = 20 \times 10^6$, but using the structured grid code developed in (Azevedo, Strauss and Ferrari, 1999, Strauss and Azevedo ,1999, Strauss, 1999). A comparison between the structured and the unstructured results is shown in Figure 7. Both results were obtained using the centered spatial discretization scheme and the Baldwin and Barth turbulence closure model. The result corresponding to the unstructured mesh shown in Figure 7 is the same result presented in Figure 4 for the case using Mavriplis' artificial dissipation model. From the comparison presented in Figure 7, one can see that the results using both mesh approaches are very similar. This was expected since, besides the mesh topology, a similar formulation was used in both cases. Moreover, the unstructured mesh results are in a slightly better agreement with the experimental data.
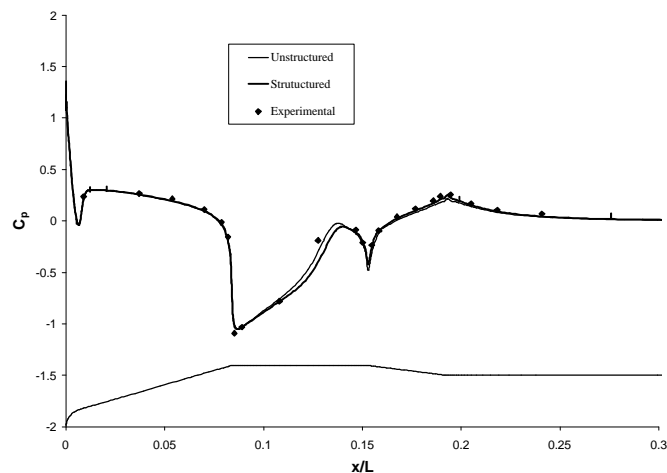

Figure 7: Comparison of pressure coefficient distributions with previous structured results ($M_{\Psi} = 0.90$ and $Re = 20 \times 10^6$).

The afterbody of the VLS second stage is treated initially as a simple base, that is, without a propulsive jet at the vehicle base. This case considers a freestream Mach number of 0.5 and a Reynolds number of 20 million. Moreover, the centered scheme with Mavriplis' artificial dissipation model is used and the turbulence effects are accounted for by the Baldwin and Barth turbulence closure model. The mesh used in this case is presented in Figure 8 and it is an extension of the forebody mesh show in Figure 3 that also includes the afterbody region. This mesh has a grid point concentration near the base region in order to capture the boundary layer close to this wall. The pressure contours in the afterbody region for this case are presented in Figure 9. These contours are very similar to the ones obtained in Refs. in (Azevedo, Strauss and Ferrari, 1999, Strauss, 1999) with the structured grid solver for the same case and using the same formulation.
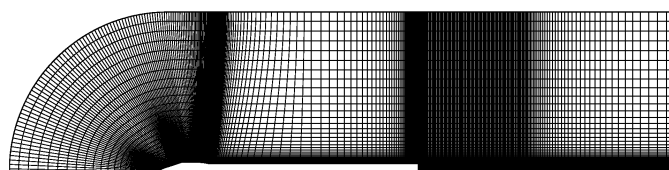

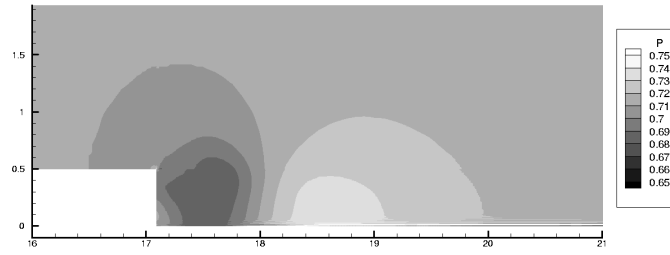Figure 8: Computational mesh including the VLS afterbody region.

Figure 9: Pressure contours in the VLS afterbody region without a propulsive jet ($M_{\infty} = 0.50$ and $Re = 20 \times 10^6$).

The results shown in Figure 9 reproduce the general trend of the expected behavior of the flow. The flow detaches from the body at the base edge and forms a recirculation bubble in the near-wake. This separated region ends in a stagnation point downstream of the base. The flowfield described can be seen in Figure 10, in which a streamline plot of the near-wake with the separated region is shown. A quantitative comparison of the results with experimental data is presented in Table 1, in terms of the axial position of the rear stagnation point. The position is measured along the centerline from the vehicle base and is presented nondimensionalized by the afterbody diameter. The experimental data was obtained from Merz, Page and Przirembel, 1978 for cylindrical afterbodies, and the errors obtained in the numerical results are of approximately 13%. These errors are not completely unexpected as Merz, Page and Przirembel, 1978 indicate that the near-wake development is dependent upon the flow conditions approaching the separation point. Therefore, as the forebody in the present work is different from the one used in the experiments of the cited reference, the boundary layer in the proximity of the separation point is also different, resulting in the differences in the near-wake. Moreover, the results obtained with the unstructured grid approach were almost coincident with the ones obtained with the structured grid approach.
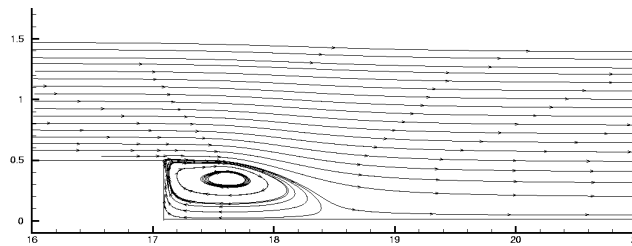

Figure 10: Streamlines in the afterbody region for the case without a propulsive jet ($M_{\infty} = 0.50$ and $Re = 20 \times 10^6$).

The cases including a base with a propulsive jet considered in this work are always of underexpanded sonic or supersonic jets, and a sketch of the expected jet structure is presented in Figure 11. Expansion waves propagate downstream from the jet exit, resulting in a jet area increase. These expansion waves reflect at the centerline as compression waves and cause a jet area reduction further downstream. The area increase is consistent with the jet acceleration, as the jet is sonic or supersonic. Moreover, the area reduction causes a jet deceleration, which is achieved by a normal shock wave, also called Mach disk. A system of oblique shock waves also forms in order to adjust the flow direction next to the jet boundaries. After the Mach disk, the flow is subsonic and therefore accelerates as a result of the area reduction, until it becomes sonic again. After that, depending on the jet to freestream pressure ratio, the complete jet structure repeats itself.
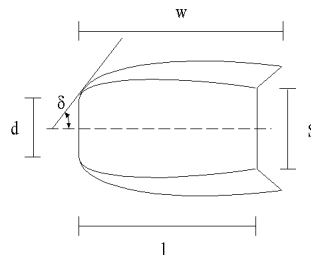

Figure 11: Sketch of the expected jet structure in the immediate vicinity of the jet exit.

Table 1: Position of rear stagnation point behind the body base. Computations consider $M_{\infty} = 0.5$ and $Re = 20 \times 10^6$ (D is the afterbody diameter and x is measured from the body base along the downstream centerline).

Case Description	Position (x/D)
Present unstructured results	1.39
Previous structured results (Strauss, 1999)	1.37
Experimental data (Merz, Page and Przirembel, 1978)	1.21

The parameters indicated in Figure 11 are used to compare the numerical and the experimental results. These parameters are: diameter of the jet exit (d), initial inclination of the jet boundary (**d**), crossflow diameter of the normal shock wave or Mach disk (S), position of the normal shock wave (l), and length of the first periodic structure (w). However, it should be noted that this is the structure of a free jet. The presence of a high speed freestream flow can change this structure as the freestream flow can inhibit the jet expansion. Since most of the experimental results found on the literature are for jets discharging in still air, some tests with very low freestream Mach numbers were performed for comparison. However, the real interest of this work is on supersonic freestream conditions, thus cases with these conditions will also be shown. The computational mesh used for the jet cases is presented in Figure 12, which shows only the afterbody region. This mesh is similar to the mesh shown in Figure 8, nevertheless this grid has a more uniform point distribution, with less refinement in the near-wake in the direction normal to the base.
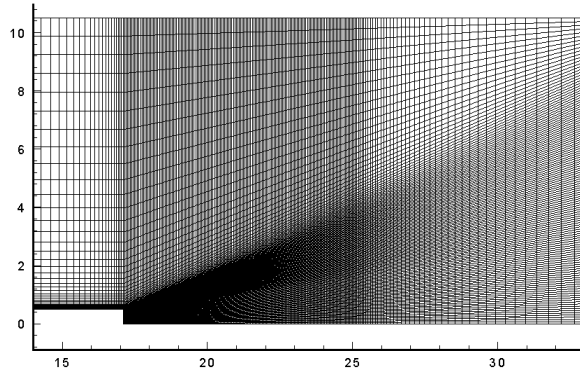

Figure 12: Computational mesh in the afterbody region for the cases including a propulsive jet on the vehicle base.

In order to simulate free jet conditions, a freestream Mach number equal to zero should be used. However, the nondimensionalization adopted yields terms which are divided by the freestream Mach number and, therefore, $M_\yen$ cannot be equal to zero to avoid numerical problems. Hence, $M_\yen = 0.01$ was chosen for the free jet cases. The Mach number contours for a case, with $M_\infty = 0.01$, $M_{jet} = 1.0$, $p_{jet} = 10\ p_\yen$, $T_{jet} = T_\yen$ is shown in Figure 13. In this case, as well as in all cases considering a propulsive jet, the Liou spatial discretization scheme was used. Moreover, the Baldwin and Barth turbulence closure model was used to properly capture the turbulence effects. An excellent qualitative agreement has been obtained between the numerical solution and the expected jet structure shown in Figure 11. A very good quantitative agreement was also obtained, as one can see in Table 2. The experimental results shown in this table were obtained from Love, *et al*, 1959. Discrepancies between the present computational results and the experimental data are usually less than 13% for all parameters analyzed.
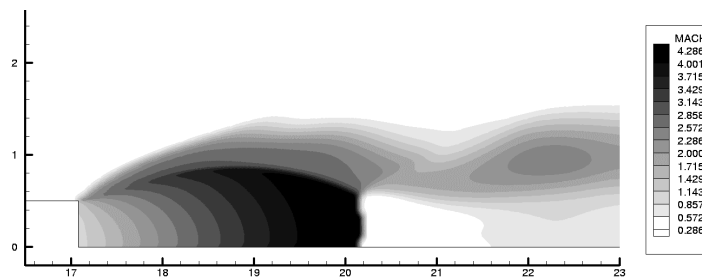

Figure 13: Mach contours in the base region for the free jet case ($M_\infty = 0.01$, $M_{jet} = 1.0$, $p_{jet} = 10\ p_\yen$, $T_{jet} = T_\yen$ and $Re = 20\times10^6$).

Table 2: Comparison of the jet parameters with experimental results for a jet discharging in still air ($M_{jet} = 1.0$, $p_{jet} = 10\ p_\yen$ and $T_{jet} = T_\yen$).

Case Description	W/d	L/d	S/d	d (°)
Present unstructured results	3.8	3.1	1.22	35.7
Previous structured results (Strauss and Azevedo, 1999, Strauss, 1999)	3.7	3.1	1.64	44.6
Experimental. data (Love, *et al*, 1959)	3.6	2.9	1.40	40.2

The freestream conditions considered for the first case run including a propulsive jet on the vehicle base and a non-still freestream were Mach number of 0.5 and Reynolds number of 20 million. The jet conditions adopted in this case where Mach number of 1.0, static pressure and temperature three and two times, respectively, the corresponding freestream quantities. The Mach number contours in the base region for this case are presented in Figure 14. In this figure a jet structure very similar to the expected one, presented in Figure 11, can be observed, showing a very good

qualitative comparison with experimental results. Furthermore, this case was also run in Strauss and Azevedo (1999) and Strauss (1999) using a structured grid approach and the results obtained in the present work were very similar to the ones shown in those references.
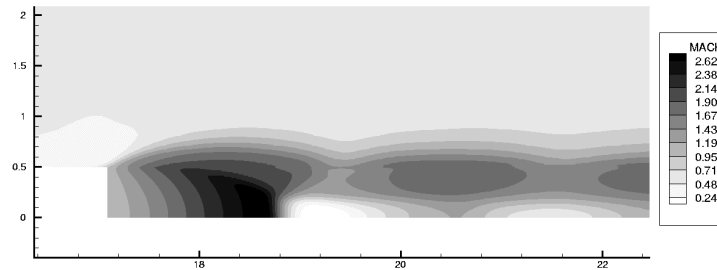

Figure 14: Mach number contours in the base region for the case including a propulsive jet ($M_\infty = 0.5$, $M_{jet} = 1.0$, $p_{jet} = 3$ p_∞, $T_{jet} = 2$ T_∞ and $Re = 20 \times 10^6$).

Flow conditions which are representative of the actual VLS flight regimes were also simulated. In this test, the corresponding freestream and jet properties result in more complex flowfields and represent a more severe simulation case. The flow properties for the VLS second stage flight conditions are $M_\infty = 4.9$, $M_{jet} = 4.0$, $p_{jet} = 112.0$ p_∞, $T_{jet} = 4.6$ T_∞ and $Re = 20 \times 10^6$. The Mach number contours for this case are shown in Figure 15. One can observe that the jet expansion is very large in this case, and the plume structure seems to be similar to what can be observed, for instance, in Figure 14. However the computational domain does not extend far enough downstream in order to capture the normal shock and all the downstream portions of the plume structure. Nevertheless, from the point of view of the accuracy of the solutions here presented, this fact should not cause any problems since the flowfield is completely supersonic throughout the entire exit plane. Therefore, whatever flow structures are supposed to appear downstream of the computational exit plane cannot influence the present computational domain. Furthermore, as one could expect, the very high jet to freestream static pressure ratio results in a strong expansion downstream of the jet exit, with local Mach numbers within the jet core reaching values as high as 12. The full range of Mach numbers within the jet is not represented in the labels of Figure 15 in order to allow the reader to see some other features of the flow. Moreover, the rapid jet expansion at its exit station causes the formation of an oblique shock wave in the external flow right at the afterbody edge. This feature can also be seen in Figure 15.
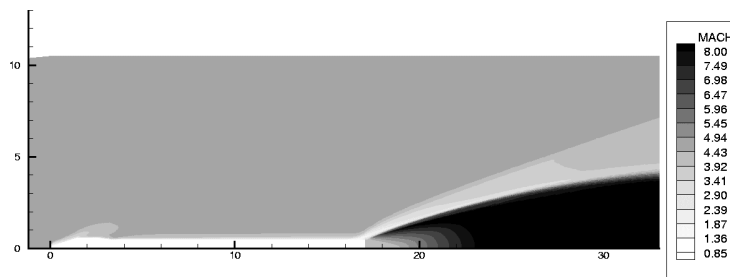

Figure 15: Mach number contours for the VLS second stage flight conditions ($M_\infty = 4.9$, $M_{jet} = 4.0$, $p_{jet} = 112.0$ p_∞, $T_{jet} = 4.6$ T_∞ and $Re = 20 \times 10^6$).

7. Concluding Remarks

The transonic flowfield around the VLS forebody was studied using a viscous turbulent formulation. Comparisons between the numerical results obtained and the experimental data showed a very good agreement in terms of pressure coefficient distribution as well as in terms of the flow features. The results with the turbulence models obtained in the present work do not present the overexpansion and overcompression observed in the inviscid results of previous work (Strauss and Azevedo, 2001). Moreover, the solutions obtained with the Liou scheme were in better agreement with the experimental results than the ones obtained with the centered scheme. Furthermore, the solutions with the centered scheme and Mavriplis' artificial dissipation model were closer to the solution with the Liou scheme than the solution with the centered scheme and Jameson and Mavriplis' artificial dissipation model.

Afterbody simulations considered cases with and without a propulsive base jet. The results without a propulsive jet obtained in the present work were compared with those obtained using a structured grid approach described in Azevedo, Strauss and Ferrari (1999) and Strauss (1999) and with experimental data for general cylindrical afterbodies at zero angle of attack. The present unstructured grid results were essentially equal to the structured grid results. Moreover, the computational results reproduced the experimental data in terms of the location of the rear stagnation point. The discrepancies between computational and experimental values for this parameter were at most of 13 %.

For the cases with a propulsive jet, since the majority of the data in the literature is concerned with free jets, the simulations initially performed considered jets discharging in a still atmosphere. Due to specific details of code

implementation, this was simulated here considering an external freestream with $M_\infty = 0.01$. An extremely good qualitatively agreement was obtained with the available experimental results for free jets and the quantitative comparison of results also indicated good agreement with the available data. Discrepancies between the present computational results and the experimental data were less than 13 % for all parameters analyzed. Results with a non-zero freestream Mach number also indicated a very good qualitative agreement with the type of behavior that should be expected in this case. Although there was no experimental data to compare the present results, as in the free jet cases, the solution structures were essentially the same ones observed in the free jet cases. Furthermore, the results obtained, which also included realistic VLS second stage flight conditions, where also compared with the structured grid cases of Strauss (1999) and, again, very good agreement was obtained with these results.

8. Acknowledgement

9. References

Azevedo, J.L.F., Menezes, J.C.L., and Fico, N.G.C.R., 1995, Jr., "An Assessment of Boundary Layer Properties for Transonic and Supersonic Flows Over the VLS," AIAA Paper 95-1769-CP, *Proceedings of the 13th AIAA Applied Aerodynamics Conference*, Part 1, San Diego, CA, pp. 41-51.

Azevedo, J.L.F., Menezes, J.C.L., and Fico, N.G.C.R., Jr., 1996, "Accurate Turbulent Calculations of Transonic Launch Vehicle Flows," AIAA Paper No. 96-2484-CP*, Proceedings of the 14th AIAA Applied Aerodynamics Conference*, Part 2, New Orleans, LA, pp. 841-851.

Azevedo, J.L.F., Strauss, D., and Ferrari, M.A.S., 1999, "Viscous Multiblock Simulations of Axisymmetric Launch Vehicle Flows," *Journal of Spacecraft and Rockets*, Vol. 36, No. 4, pp. 489-498.

Strauss, D., and Azevedo, J.L.F., 1999, "A Numerical Study of Turbulent Afterbody Flows Including a Propulsive Jet," AIAA Paper No. 99-3190, *Proceedings of the 17th AIAA Applied Aerodynamics Conference*, Norfolk, VA, pp. 654-664.

Strauss, D., and Azevedo, J.L.F., 2001, "Unstructured Multigrid Simulations of Axisymmetric Inviscid Launch Vehicle Flows," AIAA Paper No. 2001-2476, 19th AIAA Applied Aerodynamics Conference, Anaheim, CA.

Liou, M.-S., 1994, "A Continuing Search for a Near-Perfect Numerical Flux Scheme. Part I: AUSM$^+$," NASA TM-106524, NASA Lewis Research Center, Cleveland, OH.

Liou, M.-S., 1996, "A Sequel to AUSM: AUSM$^+$," *Journal of Computational Physics*, Vol. 129, pp. 364-382.

Baldwin, B.S., and Barth, T.J., 1990, "A One-Equation Turbulence Transport Model for High Reynolds Number Wall-Bounded Flows," NASA TM-102847.

Spalart, P.R., and Allmaras, S.R., 1994, "A One-equation Turbulence Model for Aerodynamic Flows," *La Recherche Aérospatiale*, No. 1, pp. 5-21.

Mavriplis, D.J., 1988, "Multigrid Solution of the Two-Dimensional Euler Equations on Unstructured Triangular Meshes", *AIAA Journal*, Vol. 26, No. 7, pp. 824-831.

Pulliam, T.H., and Steger, J.L., 1980, "Implicit Finite-Difference Simulations of Three-Dimensional Compressible Flow," *AIAA Journal*, Vol. 18, No. 2, pp. 159-167.

Jameson, A., and Mavriplis, D.J., 1986, "Finite Volume Solution of the Two-Dimensional Euler Equations on a Regular Triangular Mesh", *AIAA Journal*, Vol. 24, No. 4, pp. 611-618.

Mavriplis, D.J., 1990, "Accurate Multigrid Solution of the Euler Equations on Unstructured and Adaptive Meshes", *AIAA Journal*, Vol. 28, No. 2, pp. 213-221.

Azevedo, J.L.F., and Korzenowski, H., 1998, "Comparison of Unstructured Grid Finite Volume Methods for Cold Gas Hypersonic Flow Simulations," AIAA Paper No. 98-2629*, Proceedings of the 16th AIAA Applied Aerodynamics Conference*, Albuquerque, NM, pp. 447-463.

van Leer, B., 1979, "Towards the Ultimate Conservative Difference Scheme. V. A Second-Order Sequel to Godunov's Method", *Journal of Computational Physics*, Vol. 32, No. 1, pp. 101-136.

Barth, T.J., and Jespersen, D.C., 1989, "The Design and Application of Upwind Schemes on Unstructured Meshes", AIAA Paper No. 89-0366, 27th AIAA Aerospace Sciences Meeting, Reno, NV.

Venkatakrishnan, V., 1995, "Convergence to Steady State Solutions of the Euler Equations on Unstructured Grids with Limiters", *Journal of Computational Physics*, Vol. 118, pp. 120-130.

Mavriplis, D.J., and Venkatakrishnan, V., 1994, "Agglomeration Multigrid for Viscous Turbulent Flows", AIAA Paper No. 94-2332, 25th AIAA Fluid Dynamics Conference, Colorado Springs.

Strauss, D., 1999, "Turbulent Multiblock Simulations of Axisymmetric Launch Vehicle Afterbody Flows," Graduation Project, Dept. of Aeronautical Engineering, Instituto Tecnológico de Aeronáutica, São José dos Campos, SP, Brazil.

Merz, R.A., Page, R.H., and Przirembel, C.E.G., 1978, "Subsonic Axisymmetric Near-Wake Studies," *AIAA Journal*, Vol. 16, No. 7, pp. 656-662.

Love, E.S., *et al*, 1959, "Experimental and Theoretical Studies of Axisymmetric Free Jets", NASA Tech. Rep. R-6.